Development, parameterization, and validation of a visco-plastic material model for sand with different levels of water saturation

M Grujicic[1*], **T He**[1], **B Pandurangan**[1], **W C Bell**[1], **B A Cheeseman**[2], **W N Roy**[2], and **R R Skaggs**[2]

[1]International Center for Automotive Research CU-ICAR, Department of Mechanical Engineering, Clemson University, Clemson, South Carolina, USA

[2]Army Research Laboratory – Survivability Materials Branch, Aberdeen, Proving Ground, Maryland, USA

The manuscript was received on 24 September 2008 and was accepted after revision for publication on 19 February 2009.

DOI: 10.1243/14644207JMDA237

Abstract: A new material model for sand has been developed in order to include the effects of the deformation rate and the degree of saturation on the constitutive response of this material. The model is an extension of the original high strain-rate compaction model for sand developed by Laine and Sandvik and an elastic–visco-plastic material model for sand recently proposed by Tong and Tuan in which these effects were neglected. The new material model was parameterized using the available experimental data for sand with different levels of saturation tested mechanically at different strain rates. The model is next used, within a non-linear-dynamics transient computational analysis, to study: (a) various phenomena associated with the explosion of shallow-buried and ground-laid mines and (b) the dynamic behaviour of a vehicle during an off-road ride. The computational results are then compared with the corresponding experimental results. This comparison suggested that the newly developed material model for sand captures the essential features of the dynamic behaviour of sand with different levels of saturation when subjected to realistic high and low strain-rate loading conditions.

Keywords: sand, material model, saturation level, blast loading, tire–soil interactions

1 INTRODUCTION

Recent advances in numerical-analysis capabilities, particularly the coupling of Eulerian solvers (used to model gaseous detonation products and air) and Lagrangian solvers (used to represent vehicles/platforms, tires, and soil), have allowed simulations to provide insight into complex loading created by the detonation of buried landmines as well as the assessment of the off-road (uneven-terrain) vehicle dynamics (including vehicle rollover stability, crew and on-board equipment survivability, etc.). However, a quantified understanding, through computer modelling, of both the landmine-detonation-induced loading and the resulting interactions between the detonation products, mine fragments and soil ejecta with the target structures/vehicles as well as of the off-road vehicle dynamics is still not mature. As discussed in our previous work [**1**–**3**], the lack of maturity of computer simulations of the landmine-detonation events is mainly due to inability of the currently available material models to realistically represent the response of the materials involved (primarily soil) under high-deformation, high-deformation-rate, and high-temperature conditions, and the type of conditions accompanying a landmine detonation. Similar deficiencies (primarily those related to a lack of consideration of the effect of moisture and various organic and inorganic constituents) in the soil-material models, but under lower-deformation rates, are, at least partly, responsible for inadequacies of the computer-based off-road dynamics simulations [**4**]. This is the main reason that the objective of the present work was to attempt to develop a visco-plastic material model for soil that provides a proper account for the physical and chemical make-up of the soil and is suitable for both mine-blast and off-road vehicle dynamics computational analyses.

*Corresponding author: *Department of Mechanical Engineering, Clemson University, 241, Engineering Innovation Building, Clemson, SC 29634, USA.*

email: mica@ces.clemson.edu

Report Documentation Page

Form Approved
OMB No. 0704-0188

Public reporting burden for the collection of information is estimated to average 1 hour per response, including the time for reviewing instructions, searching existing data sources, gathering and maintaining the data needed, and completing and reviewing the collection of information. Send comments regarding this burden estimate or any other aspect of this collection of information, including suggestions for reducing this burden, to Washington Headquarters Services, Directorate for Information Operations and Reports, 1215 Jefferson Davis Highway, Suite 1204, Arlington VA 22202-4302. Respondents should be aware that notwithstanding any other provision of law, no person shall be subject to a penalty for failing to comply with a collection of information if it does not display a currently valid OMB control number.

1. REPORT DATE	2. REPORT TYPE	3. DATES COVERED
2009		**00-00-2009 to 00-00-2009**

4. TITLE AND SUBTITLE	5a. CONTRACT NUMBER
Development, parameterization, and validation of a visco-plastic material model for sand with different levels of water saturation	5b. GRANT NUMBER
	5c. PROGRAM ELEMENT NUMBER
6. AUTHOR(S)	5d. PROJECT NUMBER
	5e. TASK NUMBER
	5f. WORK UNIT NUMBER
7. PERFORMING ORGANIZATION NAME(S) AND ADDRESS(ES) **Celmson University,Department of Mechanical Engineering,Clemson,SC,29634**	8. PERFORMING ORGANIZATION REPORT NUMBER
9. SPONSORING/MONITORING AGENCY NAME(S) AND ADDRESS(ES)	10. SPONSOR/MONITOR'S ACRONYM(S)
	11. SPONSOR/MONITOR'S REPORT NUMBER(S)

12. DISTRIBUTION/AVAILABILITY STATEMENT
Approved for public release; distribution unlimited

13. SUPPLEMENTARY NOTES

14. ABSTRACT

A new material model for sand has been developed in order to include the effects of the deformation rate and the degree of saturation on the constitutive response of this material. The model is an extension of the original high strain-rate compaction model for sand developed by Laine and Sandvik and an elastic?visco-plastic material model for sand recently proposed by Tong and Tuan in which these effects were neglected. The new material model was parameterized using the available experimental data for sand with different levels of saturation tested mechanically at different strain rates.The model is next used, within a non-linear-dynamics transient computational analysis, to study: (a) various phenomena associated with the explosion of shallow-buried and ground-laid mines and (b) the dynamic behaviour of a vehicle during an offroad ride. The computational results are then compared with the corresponding experimental results. This comparison suggested that the newly developed material model for sand captures the essential features of the dynamic behaviour of sand with different levels of saturation when subjected to realistic high and low strain-rate loading conditions.

15. SUBJECT TERMS

16. SECURITY CLASSIFICATION OF:			17. LIMITATION OF ABSTRACT	18. NUMBER OF PAGES	19a. NAME OF RESPONSIBLE PERSON
a. REPORT **unclassified**	b. ABSTRACT **unclassified**	c. THIS PAGE **unclassified**	**Same as Report (SAR)**	**19**	

In the present work, the problem of material model derivation and validation for 'cohesion less' sand-based soils at various saturation levels is addressed. Since this model was jointly developed by Clemson University (CU) and the Army Research Laboratory (ARL), Aberdeen, Proving Ground, MD, it will be referred to, in the remainder of the document, as the CU–ARL visco-plastic sand model.

Soil is a very complex material whose properties vary greatly with the presence/absence and relative amounts of various constituent materials (sand, clay, silt, gravel, etc.), particle sizes, and particle size distribution of the constituent materials. In addition, the moisture content and the extent of precompaction can profoundly affect the soil properties. In the mine-blast computational-analysis community, the so-called 'porous-material/compaction' model proposed by Laine and Sandvik [**5**] has been, for quite some time, the soil model that provided the best compromise between the inclusion of essential physical phenomena reflecting material response under dynamic loading and computational simplicity. However, this model was developed essentially for dry sand and, as demonstrated by many researchers (e.g. references [**6**] to [**8**]), cannot account for the effects of moisture, clay, and/or gravel in soil. To overcome these deficiencies of the original porous-material/compaction model, CU and the ARL jointly developed [**9**–**13**] and subsequently parameterized (using the results of a detailed investigation of dynamic response of sand at different saturation levels, as carried out by researchers at the Cavendish Laboratory, Cambridge, UK [**14**, **15**]) a series of CU–ARL sand models capable of capturing the effect of moisture, clay and gravel.

The aforementioned CU–ARL soil material models were all rate-independent elastic–plastic in nature and optimized with respect to the large-strain/high-deformation-rate/high-pressure conditions encountered during detonation of landmines buried in soil. As such these models are not suitable for use in the analysis of off-road tire–soil interactions (critical for the rough-terrain vehicle dynamics and stability analyses). Consequently, an attempt is made in the present work to use the basic understanding of sand dynamic behaviour and data acquired during the development of the CU–ARL sand model in order to extend this model to the deformation regimes encountered during off-road tire–soil interactions.

Sand has generally a complex structure consisting of mineral solid particles that form a skeleton. The relative volume fractions of the three constituent materials in the sand (the solid mineral particles, water, and air) are generally quantified by the porosity, α_{por}, and the degree of saturation (saturation ratio), β_{sat}, which are respectively defined as

$$\alpha_{\text{por}} = \frac{V_{\text{p}}}{V} \tag{1}$$

and

$$\beta_{\text{sat}} = \frac{V_{\text{w}}}{V_{\text{p}}} \tag{2}$$

where V_{p} is the volume of voids (pores), V_{w} is the volume of water, and V is the total volume.

Deformation of the sand is generally believed to involve two main basic mechanisms [**16**, **17**]: (a) elastic deformation (at low-pressure levels) and fracture (at high-pressure levels) of the inter-particle bonds and (b) elastic and plastic deformations of the three constituent materials (sand particle, water, and air) in the sand. The relative contributions of these two deformation mechanisms as well as their behaviour are affected primarily by the degree of saturation of sand and the deformation rate. Specifically, in dry sand, the first mechanism controls the sand deformation at low pressures while the second mechanism is dominant at high pressures and the effect of deformation rate is of a second order. In sharp contrast, in saturated sand, very low inter-particle friction diminishes the role of the first deformation mechanism. On the other hand, the rate of deformation plays an important role. At low deformation rates, the water/air residing in the sand pores is squeezed out during deformation and, consequently, the deformation of the sand is controlled by the deformation of the solid mineral particles. At high pressures, on the other hand, water/air is trapped within the sand pores and the deformation of the sand is controlled by the deformation and the volume fractions of each of the three constituent phases. Thus, for a material model for sand, such as the CU–ARL visco-plastic sand model developed in the present work, to be considered as realistic (i.e. of high fidelity), it should be able to reflect these differences in the mechanical response of sand under different pressure and strain-rate loading conditions. In addition, removal of the main deficiencies of the so-called 'effective stress approach' [**16**–**21**] (i.e. the inability of this approach to account for: (a) deformation of the solid particles under shock loads and (b) for the fact that due to a very short duration of shock loading, water may become trapped in soil pores and provide additional load support) is also emphasized in the present work.

The organization of the article is as follows. A brief overview of the prior elastic–plastic and elastic–visco-plastic material models for sand is provided in section 2.1. Determination of the material evolution during loading and numerical solution of the associated governing equations are discussed in sections 2.2 and 2.3, respectively. Derivation and parameterization of the newly developed CU–ARL visco-plastic sand material model are presented in section 2.4. Validation of the same model against a set of high-deformation-rate (landmine blast) and low-deformation rate (off-road vehicle dynamics) results is given in section 3.

A brief summary and the conclusions obtained in the present work are discussed in section 4.

2 MODEL DEVELOPMENT AND COMPUTATIONAL PROCEDURE

In the following subsections of the present section, a description will be provided of some earlier sand material models and of the CU–ARL visco-plastic sand model. It should be first recognized that since these models are of an either elastic–plastic or elastic–visco-plastic nature, they are composed of the following three main components: (a) a yield function that defines the stress based condition(s) that must be satisfied before plastic–visco-plastic yielding can begin; (b) a material constitutive relation that governs the evolution of the yield function during elastic–visco-plastic deformation; and (c) a flow rule describing the evolution of the plastic-strain components during plastic deformation.

2.1 Prior sand modelling efforts

2.1.1 Yield criterion

In most early investigations of mine blast and off-road vehicle dynamics problems, the mechanical response of soils was modelled using the rate-independent elastic–ideal-plastic Drucker–Prager model [**21**, **22**] within which the yield function is defined as

$$f(J_2, I_1) = \sqrt{J_2} - \alpha + \theta I_1 \tag{3}$$

where I_1 and J_2 are the first and the second invariant of the total stress and the stress deviator, respectively, while α is the zero-pressure (shear) cohesive strength parameter and θ is a friction-angle-dependent coefficient. Plastic yielding occurs when $f(J_2, I_1) \geqslant 0$. It should be noted that, equation (3) reduces to the standard von Mises yield function when $\theta = 0$. Also, equation (3) simply accounts for the fact that inter-particle cohesion imparts a zero-pressure shear strength (α) to the soil, while the application of confining pressure ($P = -I_1/3$) causes the effective shear strength of soil to increase (due to an increase in the inter-particle friction). It should be further noted that, throughout this article, the following stress sign convention is used: tensile stresses are assigned a positive value while compressive stresses are negative. A schematic of the Drucker–Prager model, equation (3), is given in Fig. 1(a).

Early applications of the original Drucker–Prager model (e.g. references [**22**] and [**23**]) in various soil-based structural analyses revealed some serious shortcomings of this model.

1. The extent of plastic dilatancy (i.e. the increase in volume) under shear loading is typically much greater than that observed experimentally (in fact in some cases, shear loading gives rise to a decrease in volume).
2. Hydrostatic loading/unloading is generally found to be accompanied by a considerable hysteresis that cannot be accounted for by the original Drucker–Prager model equation (3), in which yield function does not intersect the hydrostatic-loading I_1 axis (at high pressures) and when the hydrostatic elastic response is associated with a constant value of the bulk modulus.
3. At very high pressure levels, soil tends to behave more as a fluid-like material. Under such conditions, the shear strength of the material is not expected to vary with hydrostatic pressure. In other words, the yield function should be essentially independent of I_1 at high pressures. According to the Drucker–Prager yield function, equation (3), however, shear strength of the soil continues to increase indefinitely with an increase in pressure.

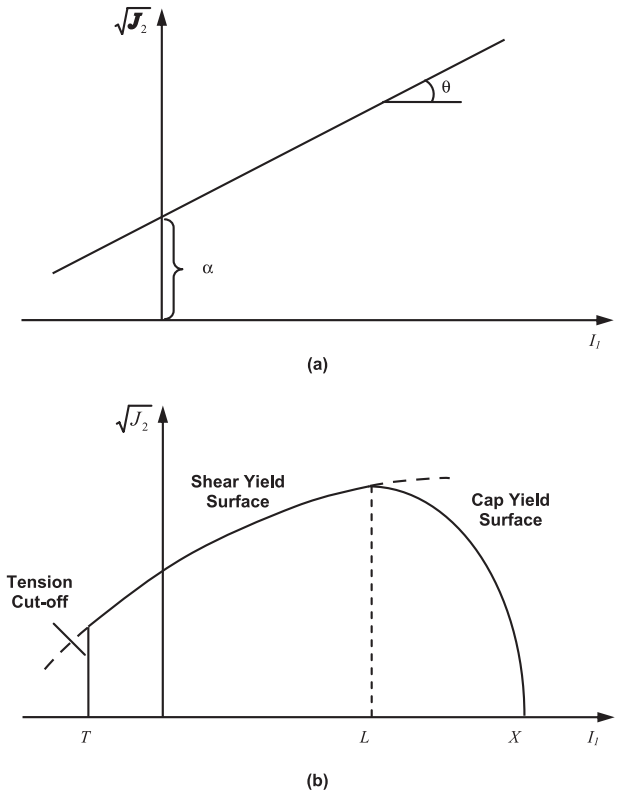

Fig. 1 Simple schematic of: (a) the original Drucker–Prager elastic–ideal-plastic yield function and (b) the modified Drucker–Prager model with a plastic-volume hardening-based moving cap

To overcome the aforementioned shortcomings of the Drucker–Prager elastic–ideal-plastic model, Dimaggio and Sandler [**23**], Sandler *et al.* [**24**], and Sandler and Rubin [**25**] proposed the addition of a moving 'cap' to the Drucker–Prager model at high-pressure values. The cap intersects the

hydrostatic loading (I_1) line (to account for the fact that plastic response of the soil can be attained under pure hydrostatic-pressure loading conditions). The position of the cap is taken to be controlled by the magnitude of the plastic volumetric strain, $\varepsilon_{\text{vol}}^{\text{pl}}$. In addition, the effect of negative pressure on the failure of soil is also accounted for by introducing a 'tension cut-off' level (the level of negative pressure at which soil fails and its shear strength i.e. $\sqrt{J_2}$ drops to zero). The pressure cut-off is denoted as T in Fig. 1(b). Furthermore, to account for the fact that, as pressure is increased, its effect on shear strength decreases, the Drucker–Prager linear (shear) yield function, equation (3), is modified as

$$f_{\text{shear}}(J_2, I_1) = \sqrt{J_2} - [\alpha - \gamma \exp(\beta I_1) - \theta I_1] \tag{4}$$

where γ and β are additional material parameters.

The cap portion of the yield function is assumed to be elliptical as

$$f_{\text{cap}}\left(J_2, I_1, \varepsilon_{\text{vol}}^{\text{pl}}\right) = \sqrt{J_2} - \frac{1}{R}\sqrt{(X-L)^2 - (I_1 - L)^2} \tag{5}$$

where R is a material parameter (a ratio of the horizontal and the vertical axes of the ellipse), while $X(\varepsilon_{\text{vol}}^{\text{pl}})$ and $L(\varepsilon_{\text{vol}}^{\text{pl}})$ are the plastic-volumetric-strain-dependent intersection of the cap yield function and the I_1 axis and the plastic volumetric-strain dependent initial value of I_1 for the cap yield-function.

2.1.2 Constitutive relation

To completely define the position of the cap yield function (which changes as a result of plastic deformation), a plastic-volumetric-strain-dependent hardening parameter, k (the value of I_1 corresponding to the centre of the cap yield-function ellipse) is used. This parameter is defined using the following function

$$\frac{X\left(\varepsilon_{\text{vol}}^{\text{pl}}\right) - k}{R} = \alpha - \gamma \exp(\beta I_1) - \theta I_1 \tag{6}$$

while the relationship between k and L is given as

$$\begin{cases} L = k, & \text{if } k > 0 \\ L = 0, & \text{if } k \leqslant 0 \end{cases} \tag{7}$$

and the plastic volumetric-strain dependence of X is furthermore defined as

$$X\left(\varepsilon_{\text{vol}}^{\text{pl}}\right) = \frac{1}{D}\ln\left(1 + \frac{\varepsilon_{\text{vol}}^{\text{pl}}}{W}\right) - X_0 \tag{8}$$

with D, W, and $X_0 = X(\varepsilon_{\text{vol}}^{\text{pl}} = 0)$ being material parameters for the cap yield-function. It should be noted that the portions of the yield surface associated with shear and tensile cut-off are assumed to be 'ideal plastic', i.e. not to evolve during plastic deformation.

2.1.3 Flow rule

The third component of the material model is the flow rule, which specifies the evolution of the inelastic strain components during deformation. For an elastic–plastic material-model formulation, a 'normality' flow rule is generally adopted, which can be defined (in a rate form) as

$$\dot{\boldsymbol{\varepsilon}}^{\text{pl}} = \dot{\lambda}\frac{\partial f}{\partial \boldsymbol{\sigma}} \tag{9}$$

where a raised dot is used to define the time derivative, superscript pl stands for plastic, $\dot{\lambda}$ is a plastic multiplier, while $\boldsymbol{\varepsilon}$ and $\boldsymbol{\sigma}$ are the strain and Cauchy stress (6×1) column vectors. Equation (9) simply states that the plastic deformation takes place in a direction which is normal to the surface defined by the yield function f (i.e. to the yield surface).

Equation (9) can be rewritten in form of the increments of the plastic strain components, $\Delta\boldsymbol{\varepsilon}^{pl}$, by multiplying both sides of equation (9) by Δt (a small time increment). For a rate-independent (i.e. inviscid) plastic material, $\Delta\lambda = \dot{\lambda}\Delta t$ is constant and is computed (as will be shown in next section) using the condition that the (new) stress state (i.e. the stress state at the end of an elastic–plastic loading step of the duration Δt) satisfies the $f(\boldsymbol{\sigma}) = 0$ condition. In the case of visco-plastic materials, on the other hand, $\Delta\lambda$ is not constant and is usually defined as [**26**]

$$\Delta\lambda = \eta\phi(f)\Delta t \tag{10}$$

where η is material constant commonly referred to a fluidity parameter and $\phi(f)$ is defined as

$$\begin{cases} \phi(f) = \left(\dfrac{f}{f_0}\right)^N, & \text{if } f > 0 \\ \phi(f) = 0, & \text{if } f \leqslant 0 \end{cases} \tag{11}$$

where f_0 and N are normalizing constants with the units of f and an exponent, respectively. Since, in accordance with equation (11), $\Delta\lambda$ scales with Δt, and there is no requirement that the new stress state satisfies the $f(\boldsymbol{\sigma}) = 0$ condition, the inelastic response of the corresponding material becomes rate (i.e. time) dependent (i.e. the material become visco-plastic).

2.2 Material-state integration procedure

In this section, a brief description is provided of the standard procedure that is used to evaluate the response of an elastic–plastic or an elastic–visco-plastic material subjected to a general state of loading. Since the sand model developed in this work is of an elastic–visco-plastic nature, the procedure provided below is given for such a material while, where needed, differences with the elastic–plastic behaviour are emphasized.

First, the total strain increment $\Delta\boldsymbol{\varepsilon}$ can be decomposed into its elastic $\Delta\boldsymbol{\varepsilon}^{\mathrm{el}}$ and visco-plastic $\Delta\boldsymbol{\varepsilon}^{\mathrm{vp}}$ as

$$\dot{\boldsymbol{\varepsilon}} = \dot{\boldsymbol{\varepsilon}}^{\mathrm{el}} + \dot{\boldsymbol{\varepsilon}}^{\mathrm{vp}} \tag{12}$$

Next, the stress at the end of an elastic–visco-plastic deformation step (time $= t + \Delta t$) is defined in terms of its value at the beginning of the same loading step (time $= t$) as

$$\boldsymbol{\sigma}_{t+\Delta t} = \boldsymbol{\sigma}_t + C(\Delta\boldsymbol{\varepsilon} - \Delta\boldsymbol{\varepsilon}^{\mathrm{vp}}) \tag{13}$$

where C is the 6×6 elastic stiffness matrix and

$$\Delta\boldsymbol{\varepsilon}^{\mathrm{vp}} = \left[(1-\chi)\dot{\boldsymbol{\varepsilon}}_t^{\mathrm{vp}} + \chi\dot{\boldsymbol{\varepsilon}}_{t+\Delta t}^{\mathrm{vp}}\right]\Delta t \tag{14}$$

where $0 \leqslant \chi \leqslant 1$ is an adjustable parameter and $\chi = 0.0$ corresponds to the fully explicit formulation, while $\chi = 1.0$ corresponds to the fully implicit formulation. The value of χ controls the stability of the numerical procedure and when $\chi \leqslant 0.5$ the procedure is conditionally stable, while when $\chi > 0.5$ it is unconditionally stable (i.e. it is stable for any value of the time increment Δt).

In the fully-implicit procedure ($\chi = 1.0$), which is considered below, the visco-plastic strain increment is defined as

$$\Delta\boldsymbol{\varepsilon}_{t+\Delta t}^{\mathrm{vp}} = \Delta\lambda_{t+\Delta t}\left.\frac{\partial f}{\partial\boldsymbol{\sigma}}\right|_{t+\Delta t} = \eta\phi(f_{t+\Delta t})\Delta t\left.\frac{\partial f}{\partial\boldsymbol{\sigma}}\right|_{t+\Delta t} \tag{15}$$

When equation (15) is plugged into equation (13), a system of six non-linear algebraic equations with six unknown components of $\boldsymbol{\sigma}_{t+\Delta t}$ is attained. While one of the standard routines can be invoked to solve this equation system, a computationally more efficient procedure is presented below [**26**].

When a material is elastic–plastic, the equation (4) becomes

$$\Delta\boldsymbol{\varepsilon}_{t+\Delta t}^{\mathrm{pl}} = \dot{\boldsymbol{\varepsilon}}_{t+\Delta t}^{\mathrm{pl}}\Delta t = \Delta\lambda_{t+\Delta t}\left.\frac{\partial f}{\partial\boldsymbol{\sigma}}\right|_{t+\Delta t} \tag{16}$$

and when equation (16) is plugged into equation (13), a system of six equations with seven unknowns ($\boldsymbol{\sigma}_{t+\Delta t}$, $\Delta\lambda_{t+\Delta t}$) is attained. In this case, the seventh equation is obtained by setting $f(\boldsymbol{\sigma}_{t+\Delta t}) = 0$.

2.3 Numerical solution procedure

In this section, a brief description is provided of an efficient numerical procedure that is used to integrate the response of an elastic–visco-plastic material subjected to a general state of loading [**26**]. To solve the associated system of six equations for an elastic–visco-plastic material, equation (13) is first rewritten as

$$C^{-1}\boldsymbol{\sigma}_{t+\Delta t} + \Delta t\dot{\boldsymbol{\varepsilon}}_{t+\Delta t}^{\mathrm{vp}} = C^{-1}\boldsymbol{\sigma}_t + \Delta\boldsymbol{\varepsilon} \tag{17}$$

so that the unknowns are located on the left-hand side, while the known quantities on the right-hand side of equation (17). Using a general notation, equation (17) can then be written as

$$P_{t+\Delta t}(\boldsymbol{\sigma}_{t+\Delta t}) = q_t \tag{18}$$

Since, in accordance with equation (13), $\dot{\boldsymbol{\varepsilon}}^{\mathrm{vp}}$ is a function of stresses, $P_{t+\Delta t}$ in equation (18) is implicitly a function of $\boldsymbol{\sigma}_{t+\Delta t}$ alone.

To solve equation (18), its left-hand side is next approximated using a truncated Taylor series as

$$P_{t+\Delta t}^{i} + P_{t+\Delta t}^{\prime,i}\,\mathrm{d}\boldsymbol{\sigma}_{t+\Delta t}^{i} = q_t \tag{19}$$

where

$$P_{t+\Delta t}^{\prime,i} = \frac{\partial P_{t+\Delta t}^{i}}{\partial\boldsymbol{\sigma}_{t+\Delta t}^{i}} \tag{20}$$

and i $(= 0, 1, 2, \ldots)$ represents the iteration number and $P_{t+\Delta t}^{\prime,i}$ is also a function of $\boldsymbol{\sigma}_{t+\Delta t}^{i}$ alone.

Thus, when an initial guess is made for $\boldsymbol{\sigma}_{t+\Delta t}^{i}$, then equation (20) can be solved for $\mathrm{d}\boldsymbol{\sigma}_{t+\Delta t}^{i}$ and an updated value for stress, $\boldsymbol{\sigma}_{t+\Delta t}^{i+1}$, obtained as

$$\boldsymbol{\sigma}_{t+\Delta t}^{i+1} = \boldsymbol{\sigma}_{t+\Delta t}^{i} + \mathrm{d}\boldsymbol{\sigma}_{t+\Delta t}^{i} \tag{21}$$

Next, the total visco-plastic strain $\boldsymbol{\varepsilon}_{t+\Delta t}^{vp,i+1}$ is computed as

$$\boldsymbol{\varepsilon}_{t+\Delta t}^{\mathrm{vp},i+1} = \boldsymbol{\varepsilon}_{t+\Delta t} - C^{-1}\boldsymbol{\sigma}_{t+\Delta t}^{i+1} \tag{22}$$

and since the yield function depends on both the current values of stress state and the total visco-plastic strain (i.e. the stress state controls the values of stress invariants while the total visco-plastic strain controls the hardening-dependent cap position), it is updated as

$$f_{t+\Delta t}^{i+1} = f\left(\boldsymbol{\sigma}_{t+\Delta t}^{i+1}, \boldsymbol{\varepsilon}_{t+\Delta t}^{\mathrm{vp},i+1}\right) \tag{23}$$

Similarly, equation (15) can be used to obtain $\dot{\boldsymbol{\varepsilon}}_{t+\Delta t}^{\mathrm{vp},i+1}$ and since both $\boldsymbol{\sigma}_{t+\Delta t}^{i+1}$ and $\boldsymbol{\varepsilon}_{t+\Delta t}^{\mathrm{vp},i+1}$ are now known, $P_{t+\Delta t}^{i+1}$ and $P_{t+\Delta t}^{\prime,i+1}$ can be updated and the aforementioned procedure continued until a convergence $|\mathrm{d}\boldsymbol{\sigma}_{t+\Delta t}^{i}| \leqslant \mathrm{tol}$ is attained.

It should be noted that, as correctly pointed out by one of the reviewers of the present article, the solution method employed in the present work is a Newton–Raphson stress-based iteration scheme. There are, however, other solution procedures such as the so-called 'cutting plane' purely explicit algorithm that is based on the plastic coefficient lambda and other implicit schemes based on either stress or hardening parameters [**27**].

2.4 Derivation and parameterization of the CU–ARL visco-plastic sand model

In this section, a procedure is presented for the extension of the elastic–visco-plastic material model for sand recently proposed by Tong and Tuan [**26**] in order to include the effect of saturation level on the sand behaviour. A summary of the proposed mathematical expressions that describe the effect of degree of saturation on various parameters of the elastic–visco-plastic material model for sand is provided in Table 1. These expressions are parameterized using open-literature experimental data and a property-correlation analysis and the parameterization results are also given in Table 1. Derivation and parameterization are carried out separately for the yield function, the constitutive equation, and the visco-plastic flow rule.

2.4.1 Isotropic linear elastic response

Since the shear modulus of sand is mainly controlled by the shear stiffness of its skeleton formed by the interlocked particles, the degree of saturation is not expected to have a first-order effect on the magnitude of the shear modulus. On the other hand, since the pore-pressure in saturated sand provides additional hydrostatic pressure load-carrying capacity to the sand, the bulk modulus is expected to increase with an increase in the degree of saturation at both the low and high deformation-rates.

2.4.2 Yield criterion

As seen in Fig. 1(b), the yield surface consists of three separate parts: the shear yield surface, the cap yield surface, and the tensile cut-off limit. These are considered, one at a time, in this section.

Shear-yield surface: according to equation (4), this portion of the yield function contains four parameters: α, β, γ, and θ. α–γ is the zero-pressure shear-yield strength of the material, γ and β control the rate of loss of the pressure dependence of the shear-yield strength while θ quantifies pressure dependence of the shear-yield strength. For dry sand, these parameters were determined by Tong and Tuan [**26**] using available public-domain experimental results, e.g. references [**28**] and [**29**]. These parameters for dry sand were first verified in the present work. Next, the effect of water/moisture on the value of these parameters is considered.

Since water present in sand increases adhesion between the sand particles, the zero-pressure shear strength ($= \alpha - \gamma$) is expected to increase with an increase in the degree of saturation. However, since water also acts as an inter-particle lubricant, it reduces the inter-particle friction coefficient and, in turn, the pressure dependence of the shear strength ($= \theta$). Lastly, β (and γ) are adjusted to comply with the condition that there is a smooth transition between the shear yield and the cap yield functions.

Cap-yield function: the cap-yield function, equation (5), is essentially controlled by two parameters: X (or L) and R. X represents the (pure) pressure

Table 1 Parameterization of the CU–ARL visco-plastic sand model for sand with an initial porosity of 0.36

Parameter symbol	Unit	Equations where first used	Value/expression (dry sand)	value/expression (saturated sand)
Yield function				
α	MPa	(4)	0.0642	$0.0642(1-\beta_{sat})+0.077\beta_{sat}$
γ	MPa	(4)	0.00 589	$0.00\,589(1-\beta_{sat})+0.0062\beta_{sat}$
β	MPa^{-1}	(4)	0.34 283	0.34 283
θ	–	(4)	0.18 257	$0.18\,257(1-\beta_{sat})+0.1187\beta_{sat}$
T	MPa		0.0069	$0.0069(1-\beta_{sat})+0.0084\beta_{sat}$
Constitutive relation				
W	–	(8)	0.2142	0.2142
D	MPa^{-1}	(8)	0.00 952	0.00 952
R	–	(6)	5.0	5.0
X_0	MPa	(8)	0.01	$0.01(1-\beta_{sat})+0.0121\beta_{sat}$
Flow rule				
$\eta_{low\text{-}rate}$	μs^{-1}	(10)	0.0002	$0.0002(1-\beta_{sat})+0.00\,016\beta_{sat}$
$\eta_{high\text{-}rate}$	μs^{-1}	(10)	–	$0.002(1-\beta_{sat})+0.0016\beta_{sat}$
N	–	(11)	1.0	1.0
f_0	MPa	(11)	100 000	100 000
Isotropic linear elastic response				
G	MPa	(13)	63.85	$63.85(1-\beta_{sat})+61.28\beta_{sat}$
$K_{low\text{-}rate}$	MPa	(13)	106.4	$106.4(1-\beta_{sat})+127.68\beta_{sat}$
$K_{high\text{-}rate}$	MPa	(13)	3000.0	$3000.0(1-\beta_{sat})+3900.00\beta_{sat}$

β_{sat} = degree of saturation.

under which plastic compaction takes place. Since plastic compaction relies on the motion of sand particles, and thus is affected by inter-particle adhesion/friction, the initial value of X, X_0, is expected to increase with the corresponding zero-pressure value of the shear-yield strength. As far as the cap-yield ellipse horizontal-to-vertical axis ratio (eccentricity), R, is concerned, it is assumed that it does not change with the degree of saturation of the sand.

Tension cup-off: the tensile fracture of sand involves inter-particle bond breaking and, hence, the tensile cut-off limit, T, is expected to be governed by inter-particle adhesion and scale with the zero-pressure shear-yield strength.

2.4.3 Constitutive relation

The basic assumption used by Tong and Tuan [**26**] that only the cap position of the yield surface evolves during plastic deformation and that only the volumetric part of the plastic deformation causes the evolution of the yield surface, is retained. According to equation (8), the constitutive relation for sand contains two parameters D and W (X_0 was defined by the cap yield function). Limited experimental results available for parameterization of the CU–ARL visco-plastic sand model did not allow reliable evaluation of the effect of saturation on D and W. Consequently, in the present rendition of the model, D and W are assumed to be independent of the degree of saturation.

2.4.4 Flow rule

According to equations (10) and (11), the visco-plastic flow rule function contains three parameters: η, f_0, and N. These parameters essentially control the rate at which visco-plastic deformation takes place as a function of the driving force ($f > 0$), that is: η/f_0^N acts as a mobility term while N is a viscous-exponent factor. Since water acts as an inter-particle lubricant and, at the same time, as an inter-particle cohesion agent, the effect of water in sand on these parameters is not easy to predict. Also, the effect can be different at different deformation rates, since at high deformation rates water is trapped and less volumetric plastic deformation takes place. On the other hand, at lower deformation rates, water is typically squeezed out and more plastic compaction is observed. Limited experimental data available for model parameterization allowed only a rough assessment of the effect of the degree of saturation on the flow rule relation. Within this assessment, f_0 and N were found not to be significantly affected by the degree of saturation. Also, η was found not to be significantly affected by the degree of saturation but only in the high-deformation-rate regime. In the low-deformation-rate regime, η was found to increase significantly with the increase in degree of saturation suggesting that saturated sand tends to behave more like a plastic material.

2.4.5 Model parameterization

The procedure presented above was applied to the case of sand with an initial porosity of 0.36. The resulting parameterization of the CU–ARL visco-plastic sand model is given in Table 1.

2.5 Implementation of the CU–ARL visco-plastic sand model

The CU–ARL visco-plastic sand model described in the previous section is next implemented in the material user subroutine, VUMAT, of the commercial finite-element program ABAQUS/Explicit [**30**]. This subroutine is compiled and linked with the finite-element solver and enables ABAQUS/Explicit to obtain the needed information regarding the state of the material and the material mechanical response during each time step, for each integration point of each element. In the present work first-order eight-node general-purpose reduced-integration solid elements (ABAQUS/Explicit designation C3D8R) are used.

The essential features of the coupling between the ABAQUS/Explicit finite-element solver and the VUMAT Material User Subroutine at each time increment at each integration point of each element can be summarized as follows.

1. The corresponding previous time-increment stresses and material state variables as well as the current time-step deformation gradient are provided by the ABAQUS/Explicit finite-element solver to the material subroutine. In the present work six total strain components, the volumetric plastic strain, six visco-plastic strain-rate components, and an element-deletion status flag were used as the state variables.
2. Using the information provided in step 1, and the CU–ARL visco-plastic sand model presented in the previous section, the material stress state as well as values of the material state variables at the end of the time increment are determined within the VUMAT and returned to the ABAQUS/Explicit finite-element solver. In addition, the changes in the total internal and the inelastic energies (where appropriate) are computed and returned to the solver.

It should be noted, that the VUMAT file developed in the present work could be used with minor modifications and new parameterization for a variety of soils with different chemical make-up and granular microstructure.

3 VALIDATION OF THE CU–ARL VISCO-PLASTIC SAND MODEL IN THE HIGH-DEFORMATION-RATE REGIME

In this section, the CU–ARL visco-plastic sand model is tested by carrying out a number of computational transient non-linear dynamics analyses under high deformation-rate conditions and by comparing the computed results with their experimental counterparts. All the calculations carried out in this section were done using ABAQUS/Explicit [**30**], a general-purpose non-linear dynamics modelling and simulation software. In this section, a brief overview is given of the basic features of ABAQUS/Explicit, emphasizing the aspects of this computer program that pertain to the problem at hand.

A transient non-linear dynamics problem is analysed within ABAQUS/Explicit by solving simultaneously the governing partial differential equations for the conservation of momentum, mass, and energy along with the materials constitutive equations and the equations defining the initial and the boundary conditions. The equations mentioned above are solved numerically using a second-order accurate explicit scheme and one of the two basic mathematical approaches, the Lagrange approach and the Euler approach. The key difference between the two approaches is that within the Lagrange approach the numerical grid is attached to and moves along with the material during calculation, while within the Euler approach, the numerical grid is fixed in space and the material moves through it. Within ABAQUS/Explicit, the Lagrange approach is used. In our recent work [**9**], a brief discussion was given of how the governing differential equations and the materials constitutive models define a self-consistent system of equations for the dependent variables (nodal displacements, nodal velocities, element material densities, and element internal energy densities).

Throughout this article, the terms 'depth of burial' (DOB) and 'stand-off distance' (SOD) are used to denote distances between the mine top-face and the sand top-face and between the sand top-face and the bottom face of the target structure, respectively.

3.1 Total momentum transferred to the target structure

To assess the ability of the CU–ARL visco-plastic sand model to account for the total momentum transferred to the target structure following detonation of a ground-laid or shallow-buried mine at different saturation levels of the sand, the computational results are compared with their experimental counterparts obtained in references [**8**] and [**31**].

3.1.1 Dry sand

To assess the ability of the CU–ARL visco-plastic sand model to account for the total momentum transferred to the target structure at low saturation levels of the sand, a non-linear dynamics-based computational analysis of the interaction of detonation products, mine fragments, and sand ejecta with an instrumented horizontal mine-impulse pendulum used in reference [**8**] is carried out and the computed results compared with their experimental counterparts. Since an in-depth description of the experimental details related to the construction and utilization of the instrumented horizontal mine-impulse pendulum can be found in our recent work [**32**], they will not be presented here.

Next, a brief description is given of the computational model used to simulate the interaction of the detonation-products/soil ejecta resulting from the explosion of a shallow-buried or ground-laid mine and the instrumented horizontal mine-impulse pendulum. The computational modelling of this interaction involves two distinct steps: (a) geometrical modelling of the instrumented horizontal mine-impulse pendulum set-up and (b) a non-linear dynamics analysis of the momentum transfer from the detonation-products, the mine casing, and soil ejecta to the pendulum.

The three (pendulum, sand, and mine) computational domains used in the present study are shown in Fig. 2. The geometrical models for the various components of the pendulum were constructed using eight-node reduced-integration solid elements with sizes varying between $50 \times 50 \times 20$ mm and $100 \times 50 \times 50$ mm. An advantage was taken of the planar symmetry of the model. In other words, a vertical plane of symmetry was placed along the length of the pendulum that enabled only a half of the pendulum, the sand, and the mine to be modelled. In accordance with the instrumented horizontal mine-impulse pendulum used in reference [**8**], different sections of the pendulum were constructed using AISI 1006 steel and rolled homogenized armour (RHA) plate material. Welded joints of the different sections of the pendulum were simulated by joining the components in question.

The size and circular-disc shape of the mine computational domain were selected to match the ones for the C4 mine used in reference [**8**]. The mine computational domain was meshed using eight-node reduced-integration solid elements with a typical size of $5 \times 5 \times 5$ mm and filled with a C4 HE material.

The sand computational domain was modelled as a circular cylinder with a radius of 750 mm and a height of 400 mm. The domain was divided into three concentric subdomains. All three subdomains were meshed using eight-node reduced-integration solid elements with a typical mesh size of $5 \times 5 \times 10$ mm in

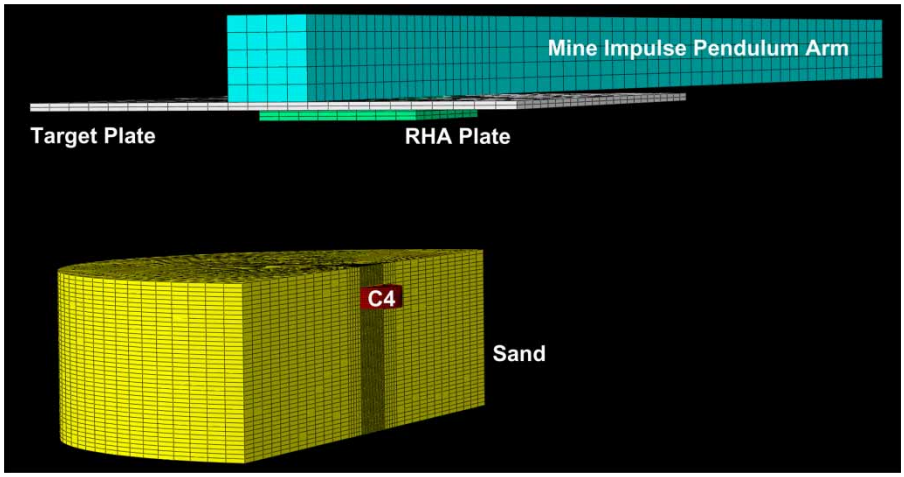

Fig. 2 Computational domains used in the analysis of total momentum transferred to the horizontal mine-impulse pendulum in the case of dry sand

the innermost subdomain and a maximum mesh size of $50 \times 50 \times 10$ mm in the outer-most sub-domain. The lateral and the bottom faces of the sand domain were lastly surrounded with eight-node CIN3D8 infinite elements in order to model far-field sand regions and avoid un-physical stress-wave reflection at the sand-domain lateral and bottom surfaces. The sand domains containing C3D8R elements were filled with CU–ARL visco-plastic sand material while the infinite elements were filled with an 'elastic' sand material with a Young's modulus and a Poisson's ratio matching those of the CU–ARL visco-plastic sand. Also, to account for non-linear behaviour of the bulk modulus at high deformation rates and large volumetric strains, and in accordance with the procedure used in the Laine and Sandvik model [**5**], a higher value (3 GPa, Table 1) of the bulk modulus was used in this portion of the work.

The mine–sand and sand–pendulum interactions were modelled using the 'hard contact pair' type of contact algorithm. Within this algorithm, contact pressures between two bodies are not transmitted unless the nodes on the 'slave surface' contact the 'master surface'. No penetration/over closure is allowed and there is no limit to the magnitude of the contact pressure that could be transmitted when the surfaces are in contact. Transmission of shear stresses across the contact interfaces is defined in terms of a static and a kinematic friction coefficient and an upper-bound shear stress limit (a maximum value of shear stress that can be transmitted before the contacting surfaces begin to slide).

A standard mesh-sensitivity analysis was carried out (the results not shown for brevity) in order to ensure that the results obtained are insensitive to the size of the elements used. Similar mesh-sensitivity analyses were carried out for the remaining studies presented in this article.

At the beginning of the simulation, the pendulum was assumed to be at rest (with the gravitational force acting downwards), while the sand and mine domains were filled with stationary materials (sand and C4, respectively). Mine detonation was initiated first along the bottom face of the mine. The motion of the pendulum was constrained to within a vertical plane and a fixed single-point constraint was applied to its pivot point. The fixed boundary conditions were applied along the circumferential and the bottom faces of the sand domain.

In accordance with the experimental procedure employed in reference [**8**], the resultant maximum angular displacement of the pendulum arm is measured and used to calculate the detonation-induced impulse on the pendulum. More details pertaining to the procedure used to assess the total mine impulse transferred to the pendulum can be found in our previous work [**32**].

An example of the results pertaining to the temporal evolution of the materials distribution in the pendulum, the sand domain and the mine domain obtained in the present work, is displayed in Figs 3(a) and (b). Clearly, upon detonation of the mine, a sand-overburden bubble is formed that expands upward and laterally. When the bubble makes contact with the RHA and the impact plates of the pendulum, the momentum transfer from sand to the pendulum begins and the pendulum swings upward.

The effect of the DOB of the mine on the total momentum transferred to the pendulum in the case of dry sand obtained in reference [**32**] is displayed in Fig. 4. Also displayed in Fig. 4 are the computational results obtained in the present work using both the original sand compaction model of Laine and Sandvik [**5**] and the present CU–ARL visco-plastic sand model. The results displayed in Fig. 4 can be summarized as follows.

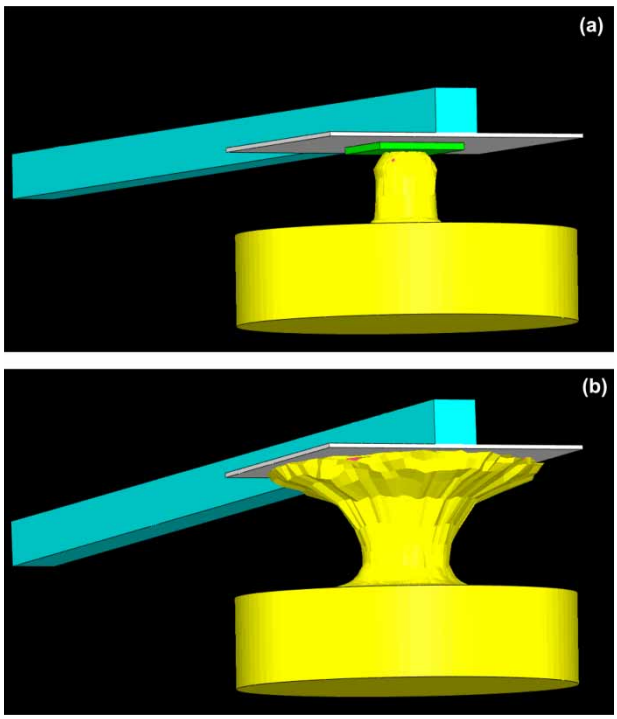

Fig. 3 An example of the temporal evolution of materials' distribution during the computational analysis of total momentum transferred to the horizontal mine-impulse pendulum in the case of dry sand. Post detonation times: (a) 230 μs and (b) 375 μs. DOB = 50 mm

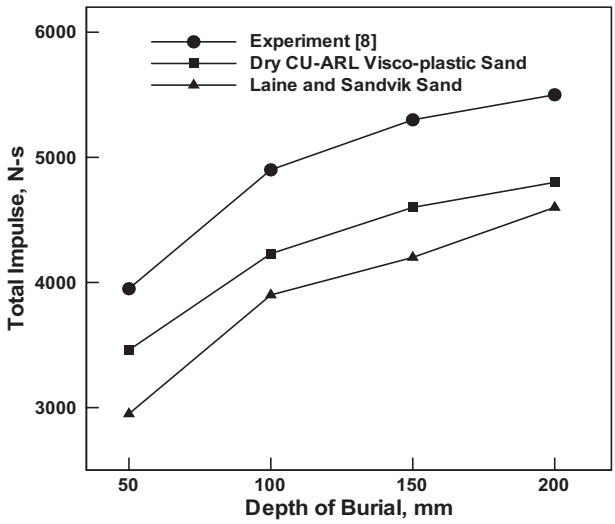

Fig. 4 The effect of mine DOB on the total impulse transferred to the horizontal mine-impulse pendulum in the case of dry sand

1. The computation/experiment agreement is somewhat improved when the original porous-material model is replaced with the CU–ARL visco-plastic sand model for all landmine detonation cases analysed.
2. Both sets of computational results, however, underpredict the total momentum transferred to the pendulum at both DOBs. This finding is not that unexpected since it is generally observed (e.g. reference [**32**]) that about 20–30 per cent of the total momentum is transferred to the target structure by blast waves generated at the sand–air interface. Since, in the present work, air surrounding the pendulum was not modelled, one could expect that the computed results pertaining to the total momentum transfer are lower than their experimental counterparts by about 20–30 per cent. This is in fact the level of computation/experiment disagreement observed in Fig. 4.
3. The general increase in the total momentum transferred to the target structure with an increase in the DOB is fairly well predicted by both sand models.
4. The effect of the DOB on the momentum transfer is directly related to the extent of sand ejection and to the energy absorbed by the sand surrounding the mine. Since rate of increase of the total momentum transferred to the pendulum decreases with an increase in the DOB, it appears that there is an optimum DOB that maximizes the lethal effect of detonation of a shallow-buried mine. This can be rationalized by the fact that as the DOB is increased the effects of detonation become more confined within the soil (the 'camouflet effect'). Determination of the optimal DOB was beyond the scope of the present work.

3.1.2 Saturated sand

To assess the ability of the CU–ARL visco-plastic sand model to account for the total momentum transferred to the target structure at high saturation levels of the sand, a non-linear dynamics-based computational analysis of the interaction of detonation products, mine fragments, and sand ejecta with a vertical impulse measurement fixture (VIMF) used in reference [**31**] is carried out and the computed results compared with their experimental counterparts. Since a detailed description of the experimental procedure related to the construction and utilization of the VIMF can be found in our recent work [**9**], they will not be presented here. Rather, it could be stated that the main component of the VIMF is a witness plate placed at a SOD from the sand right above the mine burial-site. Upon detonation of the mine, the interactions between the sand-overburden bubble and the plate results in momentum transfer that is assessed from the maximum upward velocity/displacement of the plate and the plate's mass.

The basic formulation of the computational problem dealing with the interactions between the detonation products, shell fragments, and soil ejecta (all resulting from the explosion of a shallow-buried

landmine) and the VIMF is presented next. The computational modelling of this interaction involved two distinct steps: (a) geometrical modelling of the VIMF along with the adjoining mine and sand regions and (b) the associated transient non-linear dynamics analysis of the impulse loading (momentum transfer) from the detonation products, shell fragments, and soil ejecta to the VIMF structure.

The three (VIMF witness plate, sand, and mine) computational domains used in the present study are shown in Fig. 5. Due to inherent symmetry of the model, the problem is treated as being axisymmetric. The geometrical model for the VIMF witness plate, sand, and mine were all constructed using four-node axisymmetric CAX4 solid elements with sizes varying between 2×2 mm and 30×30 mm. The lateral and the bottom faces of the sand domain were lastly surrounded with four-node CINAX4 infinite elements in order to model far-field sand regions and avoid unphysical stress-wave reflection at the sand-domain lateral and bottom surfaces. The VIMF witness plate subdomain was filled with AISI 4340 steel, the sand subdomain was filled with the present CU–ARL visco-plastic sand material or its elastic equivalent, and the mine subdomain was filled with TNT HE material. The VIMF and the mine material models and material-model parameters could be found in our previous work [**9**].

The mine–sand and sand–VIMF witness plate interactions were modelled using the aforementioned hard contact algorithm. The total mine impulse transferred to the VIMF witness plate was calculated using the maximum average vertical displacement of the plate. The remainder of the computational procedure followed the steps outlined previously in the conjunction with the mine-impulse pendulum momentum transfer analysis.

An example of the computation/experiment comparison carried out in this portion of the work is displayed in Fig. 6 in which the effect of DOB on the total momentum transferred to the VIMF witness plate is displayed for the case of a 4.54 kg, circular-disc

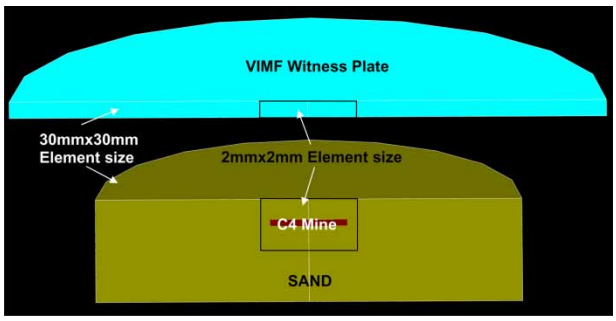

Fig. 5 Computational domains used in the analysis of total momentum transferred to the VIMF witness plate in the case of saturated sand

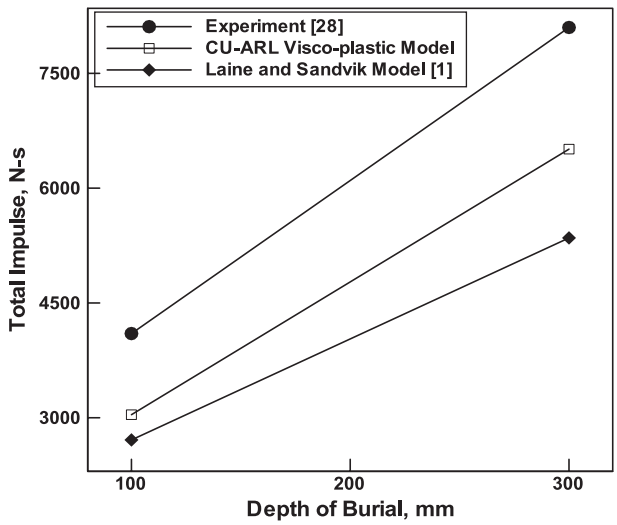

Fig. 6 The effect of mine DOB on the total impulse transferred to the VIMF witness plate in the case of saturated sand

TNT mine and SOD = 400 mm. A brief analysis of the results displayed in Fig. 6 reveals the following.

1. A significant improvement in the computation/experiment agreement is obtained when the compaction model of Laine and Sandvik [**5**] is replaced by the CU–ARL visco-plastic sand model. This finding was expected since the compaction model does not include the effect of moisture in sand. This is found to result in excessive energy absorption by the dry sand due to its compaction and in a significantly reduced extent of sand ejection (both of these effects result in reduced levels of total momentum transfer to the target structure).
2. The total momentum transfer values predicted by the CU–ARL visco-plastic sand model are again lower by ∼20–30 per cent than their experimental counterparts. As stated earlier, this discrepancy is related to lack of consideration of an air domain connecting the sand domain and the pendulum, and due to the associated neglect of the air-borne blast waves generated at the sand–air interface that impact the VIMF witness plate before sand ejecta reach the same plate.

3.2 Spatial and temporal evolution of the sand-overburden bubble

To further assess the validity of the CU–ARL visco-plastic sand model, spatial and temporal evolutions of the sand-overburden bubble (i.e. the elevated portion of sand located above the mine) following detonation of a shallow buried mine in dry and saturated sand were analysed computationally and the computational results compared with their experimental counterparts obtained in reference [**33**]. In this

section, a brief overview of the experimental setup and the procedure used in reference [**33**] is first presented.

The experiments carried out in reference [**33**] can be briefly described as follows: a 12.7 mm wall thickness cylindrical barrel with an outer diameter of 810 mm and an overall height of 710 mm is filled with sand up to its top. A 100 g cylindrical-disc shape C4 high-energy explosive (64 mm in diameter and 20 mm in height) is buried into the sand along the centre-line of the barrel with its faces parallel with the sand surface. The DOB's of 30 mm and 80 mm were investigated. The temporal evolutions of the diameter and the height of the sand-overburden bubble were determined by analysing the data obtained using high-speed X-ray photography.

The computational model developed in this portion of the work included three subdomains: (a) a steel-barrel subdomain, (b) a sand subdomain, and (c) a C4 mine subdomain. Again, the problem was considered as being axisymmetric. The steel barrel was modelled using four-node axisymmetric CAX4 solid elements with a typical size of 6.35×5 mm and filled with AISI 4340 steel. No boundary conditions were prescribed along the outer surfaces of the steel barrel. The remainder of the computational domain was constructed using a procedure analogous to the one previously described for the VIMF setup. Due to the similarity of the present computational model and the one used for the VIMF analysis, no further description of the present model will be provided and no figures dealing with the finite-element mesh used will be displayed.

An example of the typical effect of the presence of moisture on the morphology of the sand-overburden bubble is displayed in Figs 7(a) and (b). In excellent agreement with the general experimental observations, the sand bubble is shorter and wider in the case of dry sand, Fig. 7(a), and taller and narrower, Fig. 7(b), in the case of saturated sand.

3.2.1 *Dry sand*

The ability of the CU–ARL visco-plastic sand model to account for the main observations obtained during experimental investigation of landmine detonation in '*dry*' sand (average degree of saturation $\beta_{\text{sat}} < 0.15$) [**33**] is discussed first. A comparison of the computational and experimental results pertaining to the effect of SOD on the temporal evolution of the dry sand-overburden bubble height and radius is shown respectively in Figs 8(a) and (b). The results displayed in Figs 8(a) and (b) show that the overall agreement between the CU–ARL visco-plastic sand model-based results and the experimental results is reasonably good particularly in the case of 30 mm DOB. The results obtained using the compaction model showed significantly worse agreement with the experiment and, to keep clarity of the figures, are not displayed in Figs 8(a) and (b). It should be noted that, while determination of the bubble height is fairly straightforward, determination of the bubble radius was associated with some uncertainty both in the experiments and in the computational analysis.

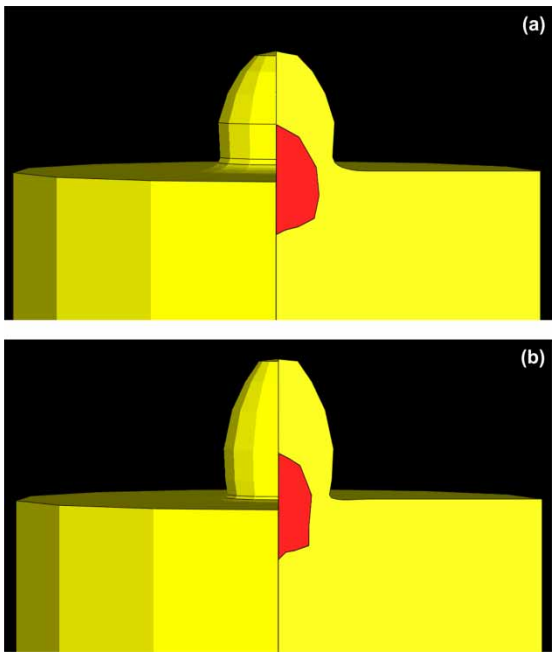

Fig. 7 Typical morphology of the sand-overburden bubble in the case of (a) dry sand and (b) saturated sand created after detonation of a 100 g C4 HE shallow-buried mine, DOB = 30 mm, and post-detonation time = 210 ms. For clarity, the steel barrel and the lower portion of the sand domain are not shown

3.2.2 *Saturated sand*

The ability of the present material model for sand to account for the main observations obtained during experimental investigation of landmine detonation in fully saturated sand (average degree of saturation $\beta_0 \sim 1.0$) [**33**] is discussed next. A comparison of the computational and experimental results pertaining to the effect of SOD on the temporal evolution of the sand-overburden bubble height and radius are shown respectively in Figs 8(c) and (d). The agreement between the computational results and their experimental counterparts displayed in Figs 8(c) and (d) is somewhat better than in the case of dry sand, Figs 8(a) and (b). This finding was also expected since the sand used in reference [**33**] contained an undisclosed amount (believed to be between 10 and 20 per cent) of clay. Since the CU–ARL visco-plastic sand model did not take into account the presence of clay and since the effect of clay is generally found to be more pronounced in dry sand (e.g. reference [**9**]), better computation/experiment agreement was expected in the case of saturated sand.

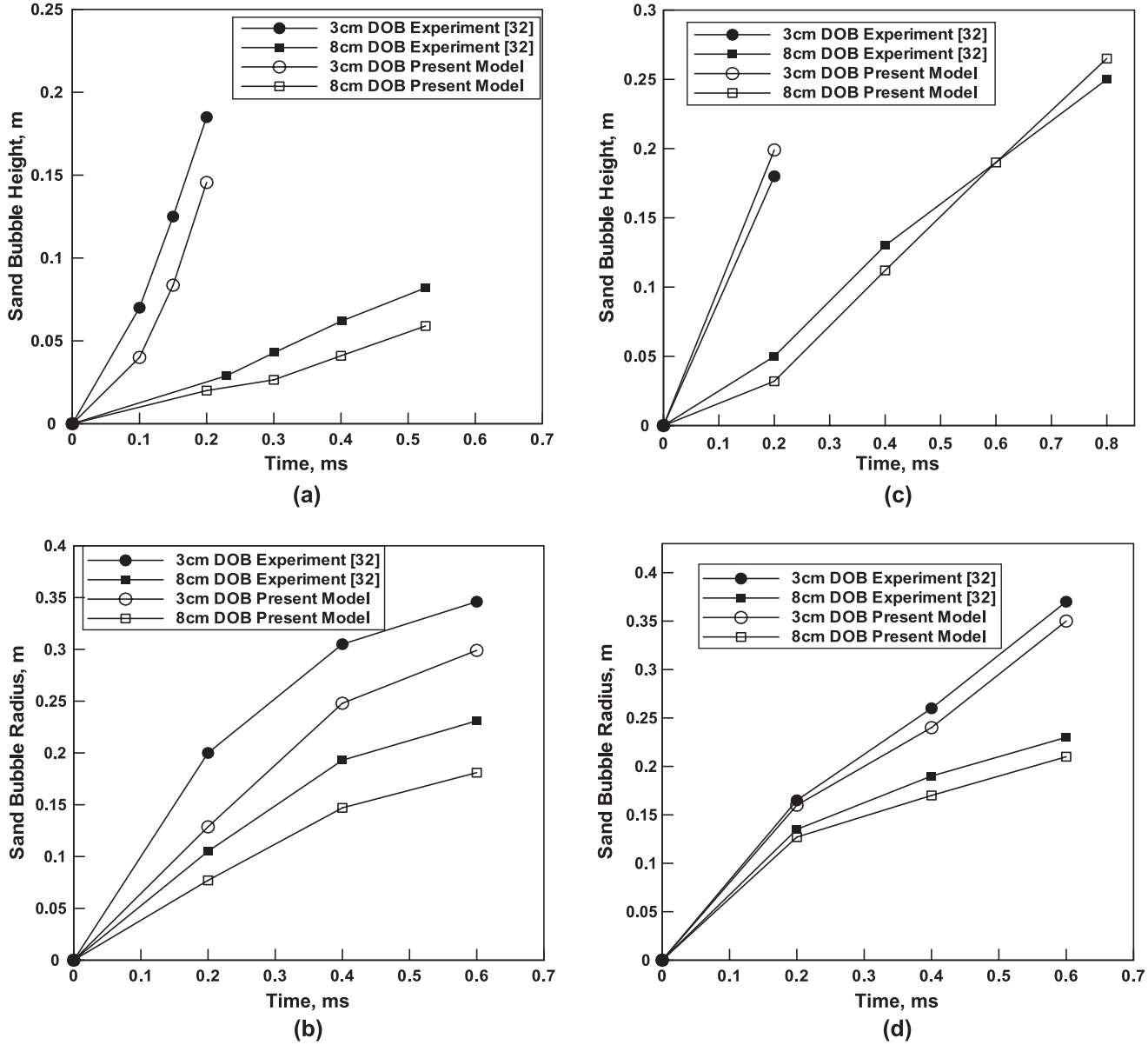

Fig. 8 Temporal evolutions of (a) and (c) sand-bubble height and (b) and (d) sand-bubble radius for (a) and (b) dry sand and (c) and (d) saturated sand at DOB's of 30 mm and 80 mm following detonation of a 100 g C4 HE shallow-buried mine

3.3 Discussion

The results presented in sections 3.1 and 3.2 suggest that the CU–ARL visco-plastic sand model when used in conjunction with the appropriate transient non-linear dynamics simulations can reasonably well account for the magnitude of the dynamic loads and for spatial distribution and temporal evolution of the sand deformation accompanying detonation of shallow-buried mines in dry or saturated sand.

This conclusion is further supported by the fact that the corresponding experimental results were associated with substantial uncertainty (typically the standard deviation was 25–30 per cent of the mean value). Also, there are additional phenomena that were not accounted for in the transient non-linear dynamics analysis of the mine detonation. For instance, blast waves, water evaporation, etc.

The extent of agreement between the CU–ARL visco-plastic sand model-based computational results and the experimental results can also be considered reasonably good considering the fact that the soils used in the three sets of experiments had varying amounts of clay and other inorganic and organic matter, as well as different average particle size and particle size distributions.

4 VALIDATION OF THE CU–ARL VISCO-PLASTIC SAND MODEL IN THE LOW DEFORMATION-RATE REGIME

In this section, the CU–ARL visco-plastic sand model is tested by carrying out a number of computational transient non-linear dynamics analyses under relatively low deformation-rate conditions and by comparing the computed results with their experimental counterparts. All the calculations carried out in this section were also done using ABAQUS/Explicit [**30**].

To validate the present CU–ARL visco-plastic sand model in the low deformation-rate regime, the model was first used in the simulations of simple uniaxial stress relaxation, uniaxial creep, and triaxial compression tests in the same way as it was done in reference [**26**]. Since these results are quite similar to the ones reported in reference [**26**], and since the tests in question are relatively simple and do not fully challenge the present material model, they are omitted here. Instead, the case of a pneumatic tire rolling on dry or fully saturated sand-based terrain is considered. This problem is of key importance to the prediction of off-road vehicle performance.

Vehicle performance on unpaved surfaces is important to the military as well as to agriculture, forestry, mining, and construction industries. The primary issues are related to the prediction of vehicle mobility (e.g. traction, drawbar pull, etc.) and to the deformation/degradation of terrain due to vehicle passage. The central problem associated with the off-road vehicle performance and terrain changes is the interaction between a deformable tire and deformable unpaved road (i.e. sand/soil). Early efforts in understanding the tire–sand interactions can be traced to Bekker, at the University of Michigan and the US Army Land Locomotion Laboratory [**34–36**]. A good overview of the research carried out in this area from the early 1960s to the late 1980s can be found in two seminal books, one by Yong *et al.* [**37**] and the other by Wong [**38**]. Over the last 25 years, there have been numerous investigations dealing with numerical modelling and simulations of tire–sand interactions. An excellent summary of these investigations can be found in Shoop [**39**].

4.1 Tire model and validation

Before the problem of tire–sand interactions can be considered, a physically-realistic tire model needs to be created and validated. Modern tires are structurally quite complex, consisting of layers of belts, plies, and bead steel imbedded in rubber. Materials are often anisotropic, and rubber compounds vary throughout the tire structure. Models developed for tire design are extremely detailed, account for each material within the tire, and enable computational engineering analyses of internal tire stresses, wear, and vibrational response. However, since, in the present work, only deformation of the tire regions in contact with sand and the tire's ability to roll over a deformable surface is of concern, a simpler model can be employed. This would provide for better computational efficiency without significant loss in essential physics of the tire–sand interactions. Towards that end, a simpler ribbed-tread tire model (described below) of the type often used for harmonic vibration modal analysis is used here.

The tire considered in the present work (the Goodyear Wrangler HT 235/75 R15) is a modern radial tire, which is composed of numerous components. Each of these components contributes to the structural behaviour of the tire and is considered either individually or en masse when creating deformable tire model. The tire direction convention used here is based on the SAE [**40**] standard definitions for vehicle dynamics. Since the tire–sand model is used only for straight-ahead pure rolling (i.e. zero slip angle) condition, the tire longitudinal axis is in the direction of travel and the lateral or transverse direction is perpendicular to travel and in the horizontal plane. Tire deflection at a given level of inflation pressure is a primary measure of the tire structural response to vertical load. Deflection is defined as the difference between the unloaded and the loaded section height and is usually normalized by the unloaded section height and reported in percentage. A thorough discussion of tire mechanics can be found in Clark [**41**].

The Goodyear Wrangler HT tire was evaluated in reference [**39**] for its deformation characteristics (i.e. the deflection and the contact area) on a rigid surface. The tire was modelled in the present work using a ribbed-tread tire model similar to that used in reference [**39**]. The side-walls and the carcass are composed of a single layer of four-node reduced-integration shell elements (S4R) with material properties representing the composite behaviour through the carcass thickness. The tread-cap is constructed using linear, hybrid continuum elements (C3D8H), with constant pressure (simulating the nearly incompressible nature of rubber). The result is a reasonable approximation of both the structural behaviour and the contact patch. The tire cross-section can be found in Fig. 43 of reference [**39**]. To take advantage of inherent symmetry of the model, tire model was cut in half using a vertical symmetry plane along the longitudinal axis. The wheel-rim and the lug-nuts are modelled as shell rigid bodies. One mass element was placed at the wheel's centre point on the symmetry plane and assigned a mass consistent with the portion of the vehicle weight supported by the wheel.

To validate the tire model a multi-step computational analysis of tire contact and rolling over a rigid-road surface was investigated first. The analysis included tire inflation, lowering to the road surface, vertical loading, and rolling (the wheel's centre point

was translated while allowing it to freely rotate about its axis due to friction, simulating a towed-wheel case). The tire–road contact was assumed to be frictionless during the loading step, and friction was added during the rolling step. During the towing step the tire was accelerated from rest to 1 m/s at a constant acceleration of 1 m/s^2 for 1 s and then it was allowed to roll at a constant velocity of 1 m/s for two more seconds.

A comparison of the computed and measured tire deflections when placed in contact with a rigid-road surface and subjected to different vertical loads (from 0 to 8000 N) at three inflation pressures (241 kPa/35 psi, 179 kPa/26 psi, and 138 kPa/15 psi) is shown in Fig. 9(a). The suggested inflation pressure for the tire is 241 kPa. Lower inflation pressures are sometimes used to reduce sinkage when driving in off-road conditions and for minimizing damage to unpaved travel surfaces. Consequently, the two lower inflation pressures were also evaluated. Performance at a range of inflation pressures is also of interest to industries using vehicles with central tire inflation systems (i.e. military, forestry, and agriculture). The results displayed in Fig. 9(a) show that the model predictions follow the same general trend as the experimental data reported in reference [**39**] for all tire pressures, with the largest difference occurring at the lower inflation pressure. This can be readily justified since undesirable tread and sidewall behaviour can occur when tires are underinflated, and these pressures and behaviours are neither within the design range nor accurately accounted for in the model. On the other hand, the agreement between data and models at the standard inflation pressure is quite good.

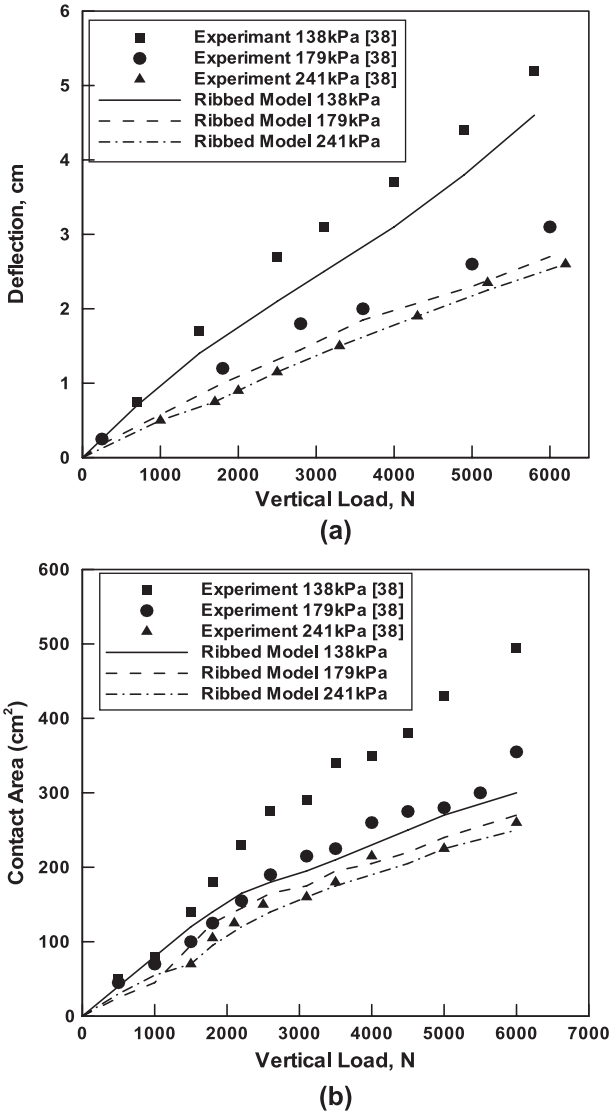

Fig. 9 The effects of vertical load and tire-inflation pressure on the (a) deflection and (b) contact-patch size for a Goodyear Wrangler HT tire in contact with a hard-road surface

A comparison between the model-predicted and the measured tire contact area results is displayed in Fig. 9(b). The contact areas are based on the perimeter of the contact, without accounting for voids within the area due to tread design. In general, the agreement between the model and measured data is reasonable.

The distributions of the contact stresses over the contact-patch area at different vertical loads and inflation pressures were also determined in the present work and the results compared with their experimental counterparts as reported in reference [**39**]. Both the computed and the measured results revealed high stress values at the tire shoulder and, to a lesser extent, along the tire centre-line. The overall computation/experiment agreement was quite good. Due to copyright restrictions, the measured contact stress distribution results could not be reproduced here and, hence, the corresponding computed results are also omitted.

As far as the tire-rolling step computational results are concerned, they were found to predict lower values of hard-surface rolling-resistance when compared to the corresponding experimental data. For example, at a tire–road friction coefficient of 0.825 (consistent with the case of an asphalt pavement), an inflation pressure of 241 kPa, and a tire velocity of 8 km/h, the computed rolling-resistance was ∼10 N while the corresponding experimental values were ∼25 N. This finding is consistent with the fact that hard-surface rolling-resistance in tires contains a substantial contribution arising from the energy dissipation associated with viscoelastic behaviour of rubber compounds in the tire. However, to improve computational efficiency, viscoelastic properties of the tire materials were not considered in the present tire model. Consequently, the computed hard-surface rolling-resistance forces reflect only the contribution of the tire–road interfacial shear. In the case of hard-surface rolling-resistance, the contributions of the viscoelastic material behaviour and the interfacial friction are generally quite comparable. In sharp contrast, when a tire

rolls over deformable terrain, the tire deforms significantly less and, consequently, the rolling-resistance is dominated by interfacial shear. Thus, despite the aforementioned computation/experiment discrepancies regarding the hard-surface rolling-resistance, the present tire model is deemed suitable for the analysis of a tire rolling over a sand road.

Based on the results presented and discussed in this section, it was concluded that the ribbed-tread tire model for the Goodyear Wrangler HT tire is a good compromise between physical reality and computational efficiency.

4.2 Analysis of tire rolling in sand

Before describing the details of the finite-element analysis used to model tire rolling in sand, a brief discussion is provided regarding tire–sand interfacial friction that plays a major role in the transfer of forces parallel to the tire–sand interface. Friction is a complex phenomenon that is controlled by various mechanical, thermal, physical, and chemical effects and, hence, is often modelled using empirical and semi-empirical laws and parameterizations. These laws/parameterizations generally apply only to the systems and conditions under which they were determined and, hence, the most reliable way to quantify friction in a given system is to measure it.

Typically, tire–road interfacial friction is measured using a vehicle traction or braking test and the results reported either as an average value of the traction/friction coefficient or as a traction force versus wheel-slip (relative tire–road velocity) curve. Both of these could be readily implemented in ABAQUS/Explicit. Unfortunately, the tire–road traction/friction data were not available for the present work. To overcome this problem, a simple Coulomb friction model based on a constant value of the friction coefficient was used and the tire–sand analysis was focused on the computation of the rolling-resistance forces (dominated by the deformation of sand) rather than on the traction effort forces (dominated by the interfacial shear/friction phenomena).

4.2.1 Finite-element model of the tire and sand-based terrain

To assess the ability of the CU–ARL visco-plastic sand model to account for the deformation behaviour of sand under lower rate yet more complex loading conditions, a transient non-linear dynamics-based computational analysis of the interaction between a Goodyear Wrangler HT tire and a deformable sand-based terrain was carried out in the present work. Since the experimental portion of this work is pending, a comparison between the computed results and their experimental counterparts could not be carried out. Instead, only the computed results are presented and discussed with respect to the general field-test observations regarding the tire–sand interactions.

The finite-element mesh model used in the present work to analyse the interactions between the Goodyear Wrangler HT tire and sand-based terrain is displayed in Fig. 10. The tire model used was described in section 4.1 and, hence, will not be discussed here. As far as the sand-based terrain model is concerned it was represented using a $2700 \times 1700 \times 450$ mm cuboidal domain. The domain was meshed using 74 000 eight-node C3D8R solid elements and 9200 eight-node CIN3D8 infinite elements. The later elements were used to model far-field sand regions and avoid stress-wave reflection at the sand-domain lateral and bottom surfaces. Finer 30 mm edge-length cubic C3D8R elements were used in the portion of the sand domain that was traversed by the rolling tire. The sand domain containing C3D8R elements was filled with CU–ARL visco-plastic sand material while the infinite elements were filled with an 'elastic' sand material with a Young's modulus and a Poisson's ratio matching those of the CU–ARL visco-plastic sand. A constant Coulomb friction coefficient was applied at the tire–sand interface.

Tire-rolling analysis was conducted by first inflating the tire, then allowing the wheel to sink into the sand due to gravity, next accelerating the wheel translationally to the desired speed, and then keeping it at a constant velocity. The last two steps were accomplished by prescribing a longitudinal velocity to the wheel centre node which creates the 'towed-wheel' conditions (i.e. the rotation of the wheel is caused by the tire–sand interfacial longitudinal shear forces).

An example of the results obtained in this portion of the work is displayed in Figs 11 to 13. The results were obtained under the following conditions: upon inflating the tire and allowing it to sink into and settle with the sand below, the tire is accelerated longitudinally at a constant acceleration of 2777.8 mm/s^2 for 1 s and then its velocity was maintained at 2777.8 mm/s (10 km/h) for another 2 s. Two cases, one involving dry

Fig. 10 Computational domains used in the rolling analysis of a Goodyear Wrangler HT tire over deformable sand-based terrain

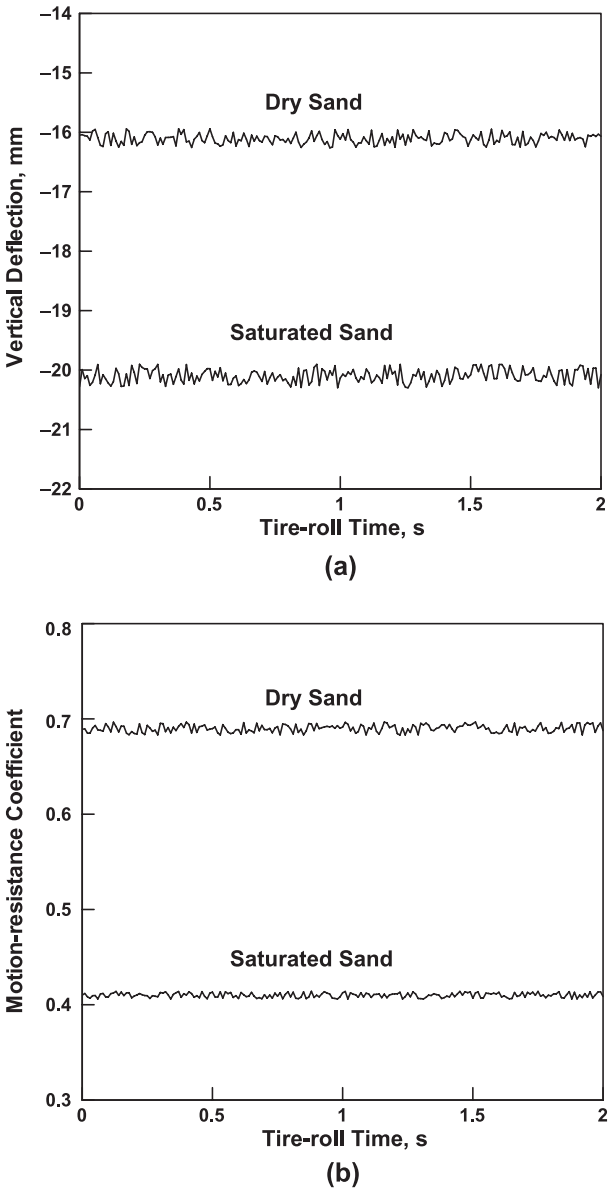

Fig. 11 Temporal evolution of: (a) vertical sinkage of the tire and (b) the motion resistance coefficient during tire roll over dry and saturated sand-based terrain

sand and the other involving saturated sand-based terrain were considered.

The results displayed in Figs 11(a) and (b) show the variation of wheel sinkage (i.e. the downward displacement of the wheeled centre) and the required drawbar pull (the reaction force acting on the wheel centre in the longitudinal direction) with respect to the tire-roll time. The results displayed in these figures pertain to the constant-velocity portion of the simulation. Furthermore, the drawbar pull force displayed in Fig. 11(b) is normalized by the normal force and the resulting quantity termed the motion-resistance coefficient. The results are reasonable since they show that a higher wheel sinkage is obtained in the case

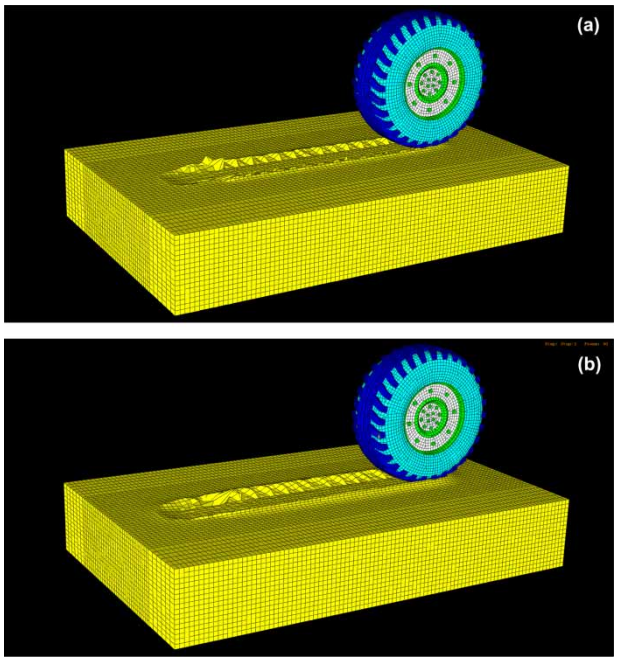

Fig. 12 Tire tracks left in: (a) dry and (b) saturated sand-based terrain

of saturated sand (mainly due to lower associated shear strength) and a higher value of the drawbar pull (mainly caused by a larger volume of the sand that needs to be displaced by the advancing wheel). As stated earlier, due to the use of a simple Coulomb friction model at the tire–sand interface and a relatively small value of the friction coefficient (0.4) the required draw bar pull is dominated by the motion resistance (i.e. by the deformation resistance of the sand). As mentioned earlier, rolling/motion resistance is the sum of the forces resisting vehicle motion. These forces are generally caused by the internal friction of the moving parts of the vehicle, the air drag, the internal resistance of the tires due to flexing of the belts and plies and viscous properties of the rubber compounds, and the added resistance due to the deformation of the road/terrain. The internal resistance of the tire was determined earlier by rolling it on a hard surface. These values were subtracted from the total motion resistance values in order to reveal the portion of the motion resistance arising from the deformation of the sand-based terrain and plotted in Fig. 11(b).

An example of the track marks left in the sand by the rolling tire is displayed in Figs 12(a) and (b) for dry and saturated sand-based terrains, respectively. Clearly the track depth is larger in the case of saturated sand and the track-side bulldozing effect is more pronounced. These observations are consistent with typical field-test observations (e.g. reference [**42**]).

Contour plots showing the distribution of the maximum shear stress in the sand beneath the tire is displayed in Figs 13(a) and (b). In both the case of dry sand and saturated-sand based terrain, the

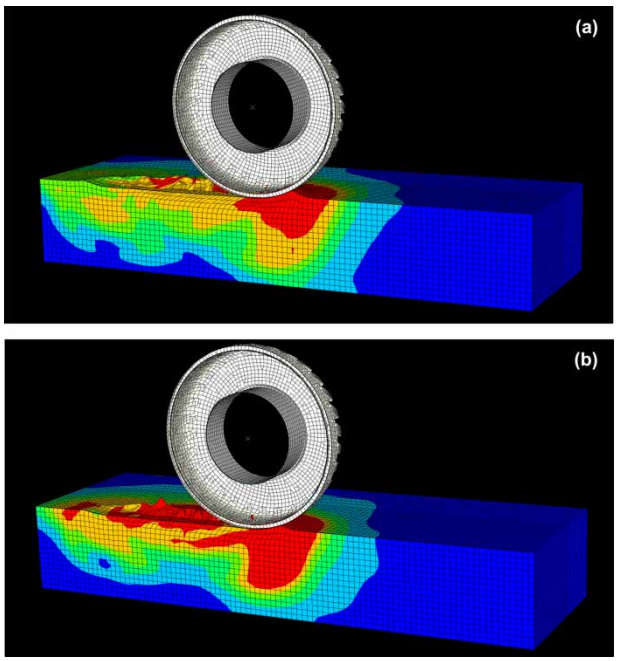

Fig. 13 Typical spatial distribution of the maximum shear stress in sand beneath the advancing wheel: (a) dry and (b) saturated sand-based terrain

largest values of the maximum shear stress are pointing downwards and away from the wheel, revealing the location where a new shearing surface begins to develop. These observations are quite consistent with experimental observations (e.g. reference [**42**]).

Based on the results presented in this section, it can be concluded that qualitatively the CU–ARL visco-plastic sand model can quite well account for typical observations made in field-tests of the off-road vehicle travel. Considering the fact that the sand model was also validated quantitatively relative to the simple laboratory uniaxial creep and stress relaxation tests, and quasi-static three-dimensional compression tests, it can be concluded that the model is quite promising. In our future communications, a more detailed quantitative comparison will be given between the computational results based on the current sand model and their experimental counterparts relative to the tire–sand interactions.

5 SUMMARY AND CONCLUSIONS

Based on the results obtained in the present work, the following main summary remarks and conclusions can be drawn.

1. The visco-plastic material model recently proposed by Tong and Tuan [**26**] has been expanded to take into account the effect of moisture and the effect of rate dependency of the bulk modulus.
2. The new model, named the CU–ARL visco-plastic sand model has been tested against a series of laboratory experiments and field-test data and observations, both in the high-deformation-rate (e.g. detonation of mine shallow-buried in sand and soil-ejecta–target-structure interactions) and in the low-deformation-rate regime (e.g. sinkage and rolling of a pneumatic tire over deformable sand-based terrain).
3. In the high-deformation-rate regime, the present sand model has been found to clearly outperform the Laine and Sandvik [**5**] sand compaction model. The latter model is very frequently used in the computational blast analysis community.
4. In the low deformation-rate regime, the CU–ARL visco-plastic sand model has been found to yield predictions regarding the extent of wheel sinkage, drawbar pull, and the distribution of stresses in sand beneath the wheel which are fully consistent with the corresponding field-test observations and measurements.

ACKNOWLEDGEMENTS

The material presented in this article is based on work supported by the US Army/CU Cooperative Agreements W911NF-04-2-0024 and W911NF-06-2-0042 and by the US Army Grant Number DAAD19-01-1-0661, and by an ARC-TARDEC research contract.

REFERENCES

1 **Grujicic, M., Pandurangan, B., Haque, I., Cheeseman, B. A.,** and **Skaggs, R. R.** A computational analysis of mine blast survivability of a commercial vehicle structure. *Multidiscip. Model. Mater. Struct.*, 2007, **4**, 431–460.

2 **Grujicic, M., Bell, W. C., Marvi, H., Haque, I., Cheeseman, B. A., Roy, W. N.,** and **Skaggs, R. R.** A computational analysis of survivability of a pick-up truck subjected to mine detonation loads. *Multidiscip. Model. Mater. Struct.*, 2008; accepted for publication.

3 **Grujicic, M., Pandurangan, B., Mocko, G. M., Hung, S. T., Cheeseman, B. A., Roy, W. N.,** and **Skaggs, R. R.** A combined multi-material Euler/Lagrange computational analysis of blast loading resulting from detonation of buried landmines. *Multidiscip. Model. Mater. Struct.*, 2008, **4**(2), 105–124.

4 **Hahn, Y., Hulbert, G., Ma, Z., Liu, Q.,** and **Lee, J.** Off-road vehicle dynamic simulation based on slip-shifted on-road tire handling model, SAE Technical Paper 08MV-5, SAE International, 2007.

5 **Laine, P.** and **Sandvik, A.** Derivation of mechanical properties for sand. In Proceedings of the 4th Asia-Pacific Conference on *Shock and impact loads on structures*, CI-Premier PTE LTD, Singapore, November 2001, pp. 361–368.

6 **Holsapple, K. A.** and **Housen, K. R.** Crater database and scaling tools, available from http://keith.aa.washinton.edu/craterdata (access date November 2004).

7 **Bergeron, D., Hlady, S.,** and **Braid, M. P.** Pendulum techniques to measure landmine blast loading. In Proceedings of the 17th International MABS Symposium, Las Vegas, USA, June 2002.

8 **Bergeron, D.** and **Tremblay, J. E.** Canadian research to characterize mine blast output. In Proceedings of the 16th International MABS Symposium, Oxford, UK, September 2000.

9 **Grujicic, M., Pandurangan, B., Huang, Y., Cheeseman, B. A., Roy, W. N.,** and **Skaggs, R. R.** Impulse loading resulting from shallow buried explosives in water-saturated sand. *Proc. IMechE, Part L: Materials: Design and Applications*, 2007, **221**(1), 21–36. DOI: 10.1243/14644207JMDA96.

10 STANAG 4569 – Protection Levels for Occupants of Logistics and Light Armored Vehicles.

11 **Grujicic, M., Pandurangan, B., Coutris, N., Cheeseman, B. A., Roy, W. N.,** and **Skaggs, R. R.** Computer-simulations based development of a high strain-rate, large-deformation, high-pressure material model for STANAG 4569 sandy gravel. *Soil Dyn. Earthq. Eng.*, 2008, **28**(12), 1045–1062.

12 **Bragov, A. M., Lomunov, A. K., Sergeichev, I. V., Tsembelis, K.,** and **Proud, W. G.** The determination of physicomechanical properties of soft soils from medium to high strain rates. *Int. J. Impact Eng.*, 2008, **35**(9), 967–976.

13 **Chapman, D. J., Tsembelis, K.,** and **Proud, W. G.** The behavior of water saturated sand under shock-loading. In Proceedings of the 2006 SEM Annual Conference and Exposition on *Experimental and applied mechanics*, 2006, vol. 2, pp. 834–840.

14 **Grujicic, M., Pandurangan, B., Cheeseman, B. A., Roy, W. N., Skaggs, R. R.,** and **Gupta, R.** Parameterization of the porous-material model for sand with various degrees of water saturation. *Soil Dyn. Earthq. Eng.*, 2008, **28**(1), 20–35.

15 **Grujicic, M., Pandurangan, B., Coutris, N., Cheeseman, B. A., Roy, W. N.,** and **Skaggs, R. R.** Derivation and validation of a material model for clayey sand for use in landmine detonation computational analysis. *Multidiscip. Model. Mater. Struct.*, 2007; accepted for publication.

16 **Wang, Z., Hao, H.,** and **Lu, Y.** A three-phase soil model for simulating stress wave propagation due to blast loading. *Int. J. Numer. Anal. Methods Geomech.*, 2004, **28**, 33–56.

17 **Wang, Z.** and **Lu, Y.** Numerical analysis on dynamic deformation mechanisms of soils under blast loading. *Soil Dyn. Earthq. Eng.*, 2003, **23**, 705–714.

18 **Loret, B.** and **Khalili, N.** A three-phase model for unsaturated soils. *Int. J. Numer. Anal. Methods Geomech.*, 2000, **24**, 893–927.

19 **Henrych, J.** *The dynamics of explosion and its use*, 1979, ch. 5 (Elsevier Publications, New York, USA).

20 **Drucker, D. C.** and **Prager, W.** Soil mechanics and plastic analysis or limit design. *Q. Appl. Math.*, 1952, **10**, 157–165.

21 **Drucker, D. C.** and **Prager, W.** On uniqueness in the theory of plasticity. *Q. Appl. Math.*, 1952, **10**, 165–175.

22 **Drucker, D. C., Gibson, R. E.,** and **Henkel, D. J.** Soil mechanics and work-hardening theories of plasticity. *Trans. ASCE*, 1957, **122**, 338–346.

23 **DiMaggio, F. L.** and **Sandler, I. S.** Material models for granular soils. *J. Eng. Mech.*, 1971, **7**, 935–950.

24 **Sandler, I. S., DiMaggio, F. L.,** and **Baladi, G. Y.** Generalized cap model for geological materials. *J. Geotech. Eng. Div. ASME*, 1976, **102**(GT7), 638–699.

25 **Sandler, I. S.** and **Rubin, D.** An algorithm and a modular subroutine the cap model. *Int. J. Numer. Anal. Method Geomech.*, 1979, **3**, 173–186.

26 **Tong, X.** and **Tuan, C. Y.** Viscoplastic cap model for soils under high strain rate loading. *J. Geotech. Geoenviron. Eng.*, 2007, **133**(2), 206–214.

27 **Wong, J. R.** and **Reece, A. R.** Prediction of rigid wheel performance based on the analysis of soil-wheel stresses. *J. Terramech.*, 1967, **4**(2), 7–25.

28 *ABAQUS version 6.8.1*, user documentation, Dassault Systems, Providence, RI, 2008.

29 **Taylor, L. C., Skaggs, R. R.,** and **Gault, W.** Vertical impulse measurements of mines buried in saturated sand. *Fragblast*, 2005, **9**(1), 19–28.

30 **Saleeb, A. F.** and **Wilt, T. E.** Analysis of the anisotropic viscoplastic-damage response of composite laminates – continuum basis and computational algorithms. *Int. J. Numer. Methods Eng.*, 2005, **36**(10), 1629–1660.

31 **Wang, J.** Simulation of landmine explosion using LSDYNA-3D software. Report DSTO-TR-1168, Aeronautical and Maritime Research Laboratory, Australia, 2001.

32 **Dobratz, B. M.** and **Crawford, P. C.** LLNL explosives handbook: properties of chemical explosives and explosive simulants. Report no. UCRL-52997, Lawrence Livermore National Laboratory, Livermore, California, 1985.

33 **Grujicic, M., Pandurangan, B., Cheeseman, B. A.,** and **Roy, W. N.** Application of the modified compaction material model to soil with various degrees of water saturation. *Shock Vibr.*, 2008, **15**, 79–99.

34 Material Science Corporation (MSC). Methodology for improved characterization of land mine explosions. Presentation on Technical Interchange Meeting of SBIR Phase II Plus Program, Contract DAAD 17-01-C-0111, Horsham, Pennsylvania, 2006.

35 **Bekker, G.** *Theory of land locomotion*, 1956 (The University of Michigan Press, Ann Arbor, Michigan).

36 **Bekker, G.** *Off-road locomotion*, 1960 (The University of Michigan Press, Ann Arbor, Michigan).

37 **Bekker, G.** *Introduction to terrain–vehicle systems*, 1969 (The University of Michigan Press, Ann Arbor, Michigan).

38 **Yong, R. N., Fattah, E. Z.,** and **Skiadas, N.** *Vehicle terrain mechanics*, 1984 (Elsevier, New York).

39 **Wong, J. Y.** *Terramechanics and off-road vehicles*, 1989 (Elsevier, New York).

40 **Shoop, S. A.** Finite element modeling of tire-terrain interaction. CRREL Technical Report, ERDC/CRREL TR-01-16, US Army Cold Regions Research and Engineering Laboratory, November 2001.

41 Society of Automotive Engineers. *SAE glossary of automotive terms*, 1992 (Warrendale, Pennsylvania).

42 **Clark, S. K.** Mechanics of pneumatic tires. US Department of Transportation, National Highway Traffic Safety Administration, 1981.